Supplementary Information for

Prediction of properties from first principles with quantitative accuracy: six representative ice phases

Qianqian Lu[1,2], Imran Ali[1,2] Jinjin Li[1,2*]

[1]National Key Laboratory of Science and Technology on Micro/Nano Fabrication, Shanghai Jiao Tong University, Shanghai, 200240, China

[2]Key Laboratory for Thin Film and Microfabrication of Ministry of Education, Department of Micro/Nano-electronics, Shanghai Jiao Tong University, Shanghai 200240, China

*Correspondence to: Jinjin Li (lijinjin@sjtu.edu.cn)

Figure 1 shows the crystal structures of ices II, VI, VII, VIII, IX and XV, where ices II, IX, VIII and XV are proton-ordered throughout their entire thermal stability range, while ices VI and VII are proton-disordered structures. Except for ice II, the lattice angles of ices VI, VII, VIII, IX and XV are all 90 degrees. In these six phases, ices II and IX contain a unique H-bond network that fills the whole volume, while the others (ices VII, VIII, VI, and XV) are made of two identical and independent networks that interpenetrate one into another. With the temperature decreasing at 0.25 GPa, the H_2O framework undergoes structural changes firstly from liquid to ice III with the ordering of the oxygen network, then from ice III to ices II and IX. Ice II has a completely proton-ordered rhombohedral lattice, while ice IX is a low-temperature proton-ordered phase with an identical tetragonal crystal structure. Upon compressing, the proton-ordered ices II and IX can be converted into proton-disordered ice VI and proton-ordered ice XV, respectively. Further compressing above 2.0 GPa, ices VI and XV will transform into proton-disordered ice VII and proton-ordered VIII, respectively. Ices VII and VIII, occupying the most part of ice phase diagram (existing from ambient pressure to ~80 GPa), consist of two interpenetrating hydrogen-bond networks, each one containing oxygen at the sites of a diamond lattice. Ices VI and VII are hydrogen-disordered and paraelectric structures, which are expected to disappear and transform into ices XV and VIII at low temperatures.

In the following, we show the details of MP2-EE-GMF predicted crystal structures, Raman/IR spectra, and vibrational frequency for ice phases II, VI, VII, VIII, IX and XV. Ice VI and VII are proton-disordered structures, while ice II, VIII, IX and XV are proton-ordered structures.

1. Ice phase II

Crystal structure

  Pressure and temperature conditions within a large proportion of the solar system's icy moons are suitable for the stability of ice II. Therefore, the physical properties of ice II are pertinent to understanding of the geophysics of icy moons influencing, amongst other things, the convective regimes in their interiors [1].The structure of ice II was first determined by Kamb in 1964, where the positions of the hydrogen atoms through small perturbations were determined using single-crystal x-ray diffraction[2]. Figure S1 shows the unit cell of ice II, which forms rhombohedral crystals with the space group of $R\bar{3}$. In ice II, all water molecules are hydrogen-bonded to four others, two as donors and two as acceptors. Ice II may exist metastably below ~100 K between ambient pressure and ~5 GPa. The crystal parameters we used are $(a,b,c,\alpha,\beta,\gamma)$ = (*7.78 Å, 7.78 Å, 7.78 Å, 113.1°, 113.1°, 113.1°*) [2].
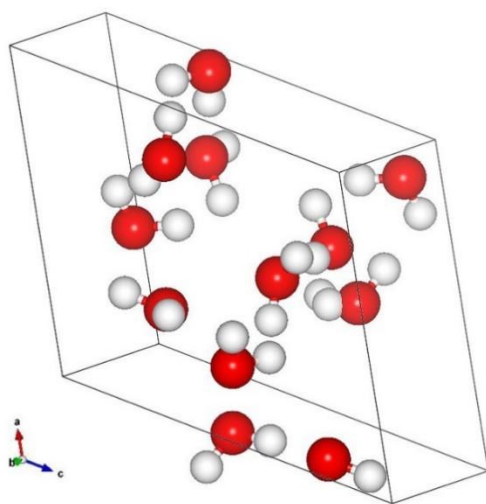
Figure S1 The crystal structure of ice II, in which the unit cell contains 12 molecules. Oxygen atoms are represented by red spheres, and hydrogen atoms are represented by smaller grey spheres, respectively.

Equations of state

Figure S2 (a) and (b) plot the calculated lattice constant and H$\cdots$O bond length as a function of the external pressure, respectively. The MP2/aug-cc-pVDZ predicts smooth pressure dependences for lattice constants and H-O bond. As shown in Figure S2 (a), the lattice constants a, b and c decrease more rapidly at lower pressures (P < 0.1 GPa) and less at higher pressures (P > 0.1 GPa), indicating that, when the crystal is compressed, it becomes stiffer as neighboring atoms beginning to experience strong repulsive interactions of the nonbonded atom-atom potentials. The pressure dependence of the H$\cdots$O bond length, drawn in Figure S2 (b), is similar to that of Figure S2 (a) as the latter is largely determined by the former. At 0 GPa, the MP2 result is in excellent agreement with the observed data. The calculated curves in Figure S2 (a) and (b) display no noticeable discontinuity. Table

S1 shows the comparison of observed[2] and calculated lattice constant (a) and volume (V) of ice II at 0.1MPa.
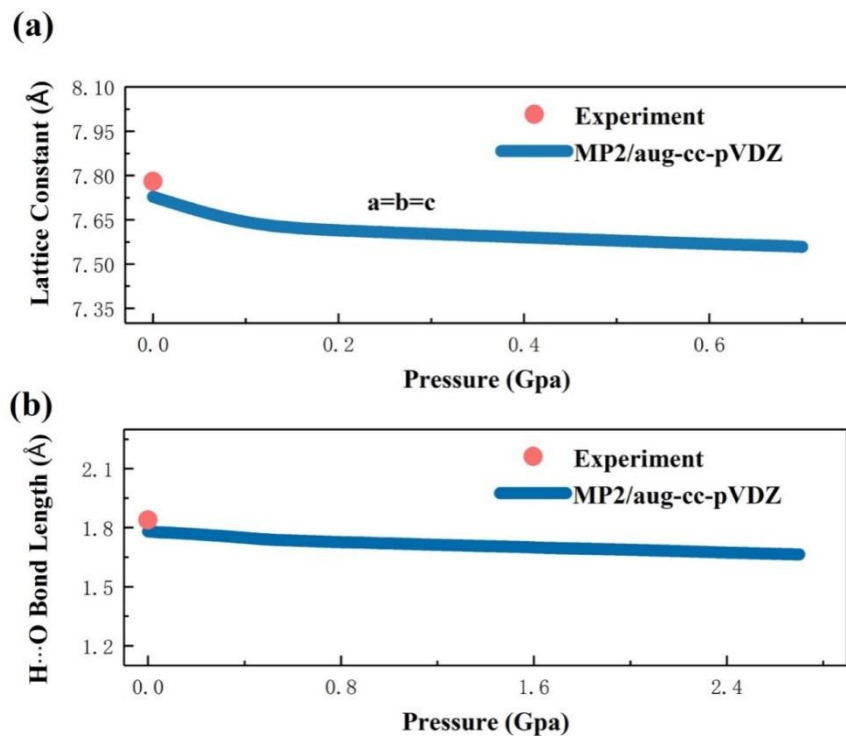
Figure S2 The pressure dependences of the lattice constant (a) and H···O bond length (b) of ice II, calculated by EE-GMF-MP2/aug-cc-pVDZ. The blue curves and red dots denote the MP2-predicted results and experiment data from Kamb *et al.* [3], respectively.

Table S1. Structural parameters of ice-II at 0.1MPa. The experiment data are taken from Kamb *et al.* [1].

Ice II	Experiment	MP2/aug-cc-pVDZ prediction
a (Å)	7.78	7.73
V (cm^{3}mol^{-1})	15.26	14.96

Vibrational spectra
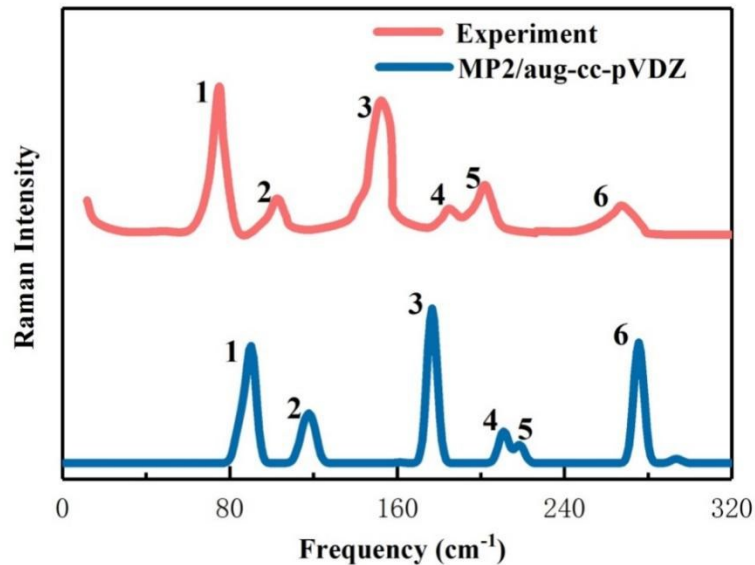
Figure S3 Calculated (blue curve) and observed [4] (red curve) Raman spectra of ice II in the librational region (low frequency) at atmosphere pressure.

Computationally reproducing the vibrational spectra with *ab initio* methods remains to be a major challenge. Figure S3 compares the observed (red curve) and calculated (blue curve) Raman spectra of ice II in the range of 0-320 cm^{-1}. There are six observed Raman bands which are assigned to the six predicted bands labeled 1-6 at atmosphere pressure. Here, the frequencies and relative intensities of six experimental Raman bands are well reproduced by EE-GMF-MP2/aug-cc-pVDZ calculation.

2. Ice phase VI
Crystal structure
Ice VI consists of two interpenetrating yet independent hydrogen-bonded networks, and has therefore been described as a "self-clathrate". Ice VI has a structure based on a space group of *P4$_2$/nmc*, which implies that the hydrogen-bonded water molecules in ice VI are fully orientationally disordered which gives rise to thousands of configurations. The structure of ice VI was confirmed by Kuhs *et al.* who performed neutron diffraction on ice VI samples under in-situ pressure conditions [5,6]. To cater to the phase transition, for the proton-disordered ice phases we select the structure that has the similar dipole moment with the neighboring phase, rather than assuming that all configurations have the same statistical weight (as Pauling and many researchers did when estimating the free energies of ice) [7-9] The crystal parameters we used are $(a,b,c,\alpha,\beta,\gamma)$=(*6.166 Å, 6.166 Å, 5.689 Å, 90°, 90°, 90°*) [4]. Figure S4 shows the unit cells of five candidate structures of ice VI.
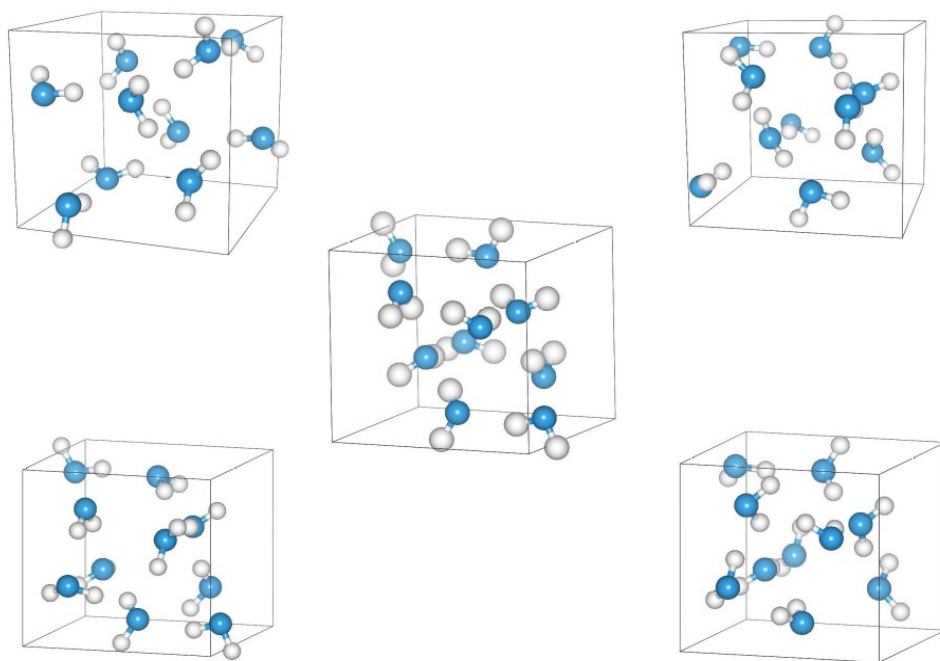
Figure S4 The possible structures of ice VI unit cell, which contains 10 water molecules. Ice VI is a proton-disordered structure and the orientation of proton has thousands of configurations with the restriction of ice rules.

Equations of state

Figure S5 compares the calculated and observed lattice constant and H···O bond length as a function of the external pressure. The red dots come from the experimental work by Kuhs *et al.* [10], which agree well with the predicted results by MP2-aug-cc-pVDZ. The constants *a* and *c* in Figure S5 (a) undergo nearly the same amount of compression, indicating that the crystal will become stiffer with the increasing of pressure. Figure S5 (b) presents the pressure dependence of the H···O distance, which exhibits shrinking behavior as the pressure increases and this ultimately leads to the decreasing of lattice constants.
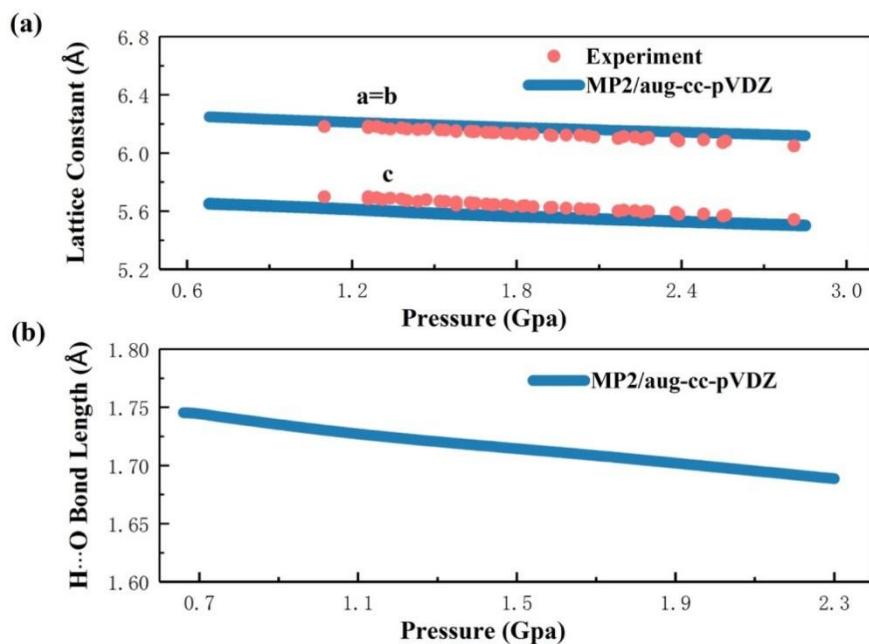
Figure S5 The pressure dependences of the lattice constant and the H⋯O bond length of ice VI calculated by EE-GMF-MP2/aug-cc-pVDZ (blue line). The red dots are the experimental data from Kuhs *et al.* [10].
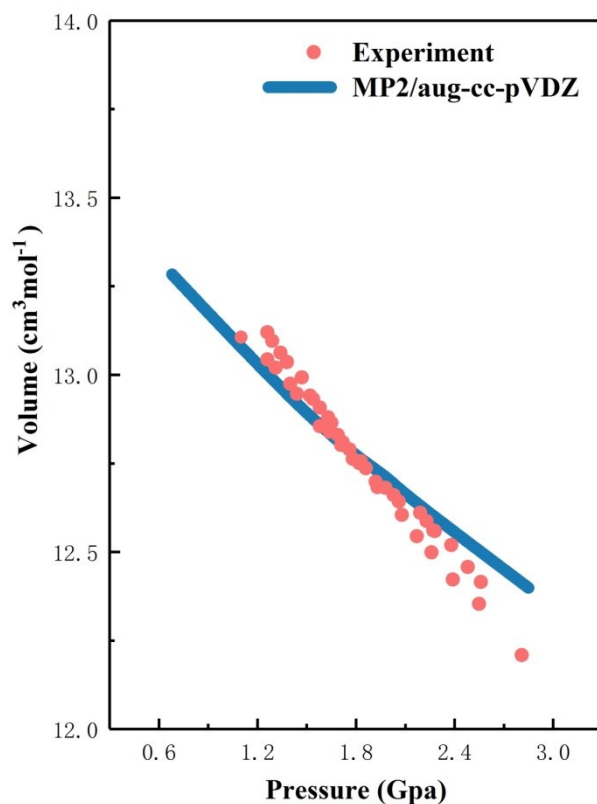
Figure S6 The unit cell volume of ice VI as a function of the pressure. The red dots are the experiment data from Kuhs *et al.* [10].

The unit cell volume is plotted as a function of the pressure (see Figure S6). The MP2-aug-cc-pVDZ predicted volumes agree well with the experimental data (the red dots in Figure S6). With the increasing of pressure, the solid ice VI becomes progressively stiffer, resisting compression. This can be explained by the fact that the atoms enter the repulsive region of the nonbonded potentials.

Vibrational spectra
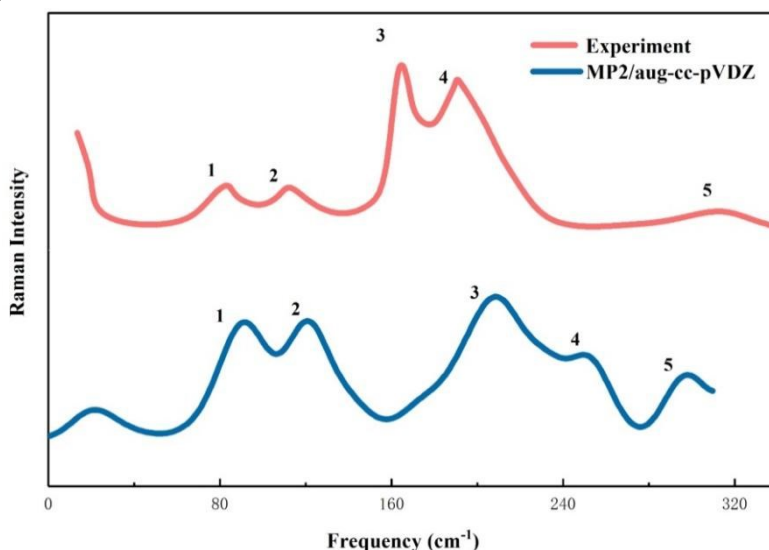
Figure S7 The observed (red curve) and calculated (blue curve) Raman spectra of phase VI in the librational region at 0.62 GPa. The observed spectra are taken from Minceva-Sukarova *et al.* [11].

The vibrational spectra are often more sensitive in probing the phase transitions and other structural changes. Figure S7 shows the experimental (red curve) and MP2-predicted (blue curve) Raman spectra at 0.62 GPa. There are five predicted Raman bands in the librational region which are assigned to the five observed bands labeled 1-5. The calculated Raman spectrum captures the overall appearance of the observed peaks reasonably well. All important bands are accounted from calculations. As shown in Figure S8, the calculated IR spectrum is compared with the experiment in the range of 70-280 cm^{-1}, where the overall spectral profile show good agreement between the experimental spectrum and MP2/aug-cc-pVDZ predicted spectrum at atmospheric pressure.
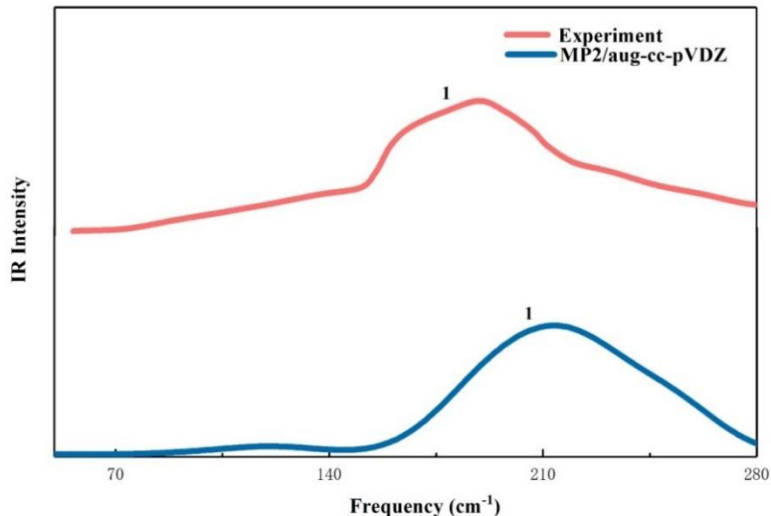
Figure S8 The observed and calculated IR spectra of ice VI at atmospheric pressure. The observed IR spectra come from Beritie *et al.* [12].

3. Ice phase VII

Crystal structure

For pressures above 2 GPa, the phase diagram is dominated by two phases of ice (see phase diagram in Figure 3), namely, Ice-VII and Ice-VIII [13-15]. The structures of these phases only differ in H-bond orientations and have slight distortions in lattice constants. Ice VII is one of the densest ice polymorphs with proton-disordered structure. It has a simple crystal structure, but its thermodynamic properties are quite interesting. In 2018, Ice VII was identified among inclusions found in the natural diamond, and because of this, ice VII has been classified as a distinct mineral [16]. The ice VII unit cell, which forms $Pn\bar{3}m$ space group, consists of two interpenetrating cubic ice lattices with hydrogen bonds passing through the center of the water hexamers and no connecting hydrogen-bonds between lattices. The proton-disordered ice VII can be ordered by simply cooling and it forms proton-ordered ice VIII below 273 K up to ~8 GPa. Above this pressure, the VII–VIII transition temperature drops rapidly. When dealing with the proton-disordered ice VII, we select the structure that obeys the ice rules and its dipole moment has the highest similarity with the corresponding ordered phase. Figure S9 shows the unit cells of five candidate structures of ice VII. The crystal parameters we used are $(a,b,c,\alpha,\beta,\gamma)$=*(6.7 Å, 6.7 Å, 6.7Å, 90°, 90°, 90°)* [5].
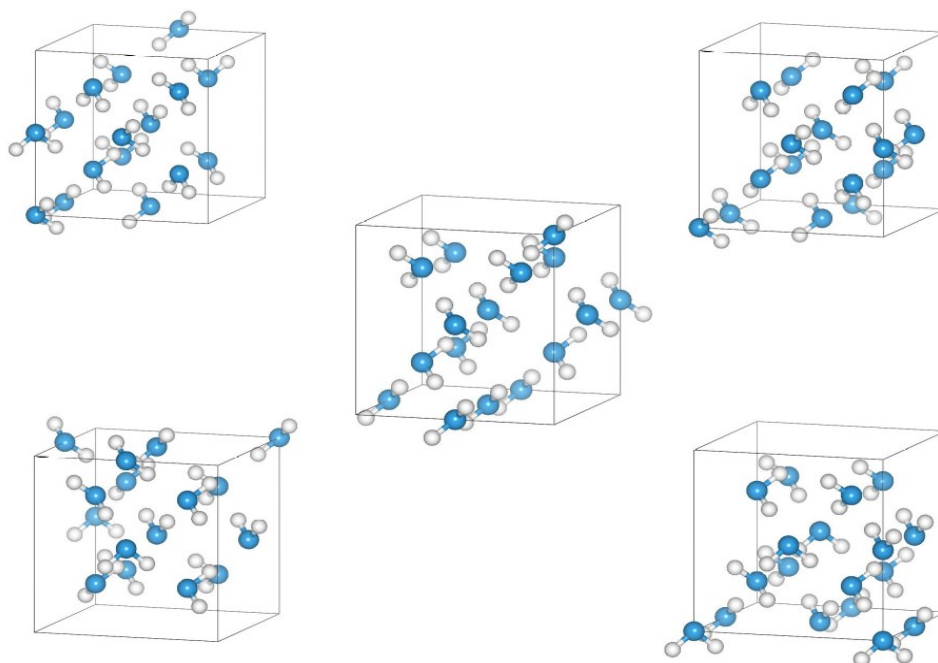
Figure S9 The unit cells of five candidate ice VII which contains 16 water molecules. Ice-VII has a cubic unit cell and H-bond orientations are considered to be random subject to the ice rules.

Equations of state

Figure S10 compares the calculated lattice constant and H···O bond length with observed data. The predicted results by MP2/aug-cc-pVDZ match the experimental lattice constants very well. The pressure-volume curve of ice VII is drawn in Figure S11. The red dots below 2.0 GPa are hypothetical data because ice VII only exists at high pressures (P > 2.0 GPa). Importantly, there is no discontinuity or any other anomaly in the calculated or observed equation of state in 0-28 GPa.
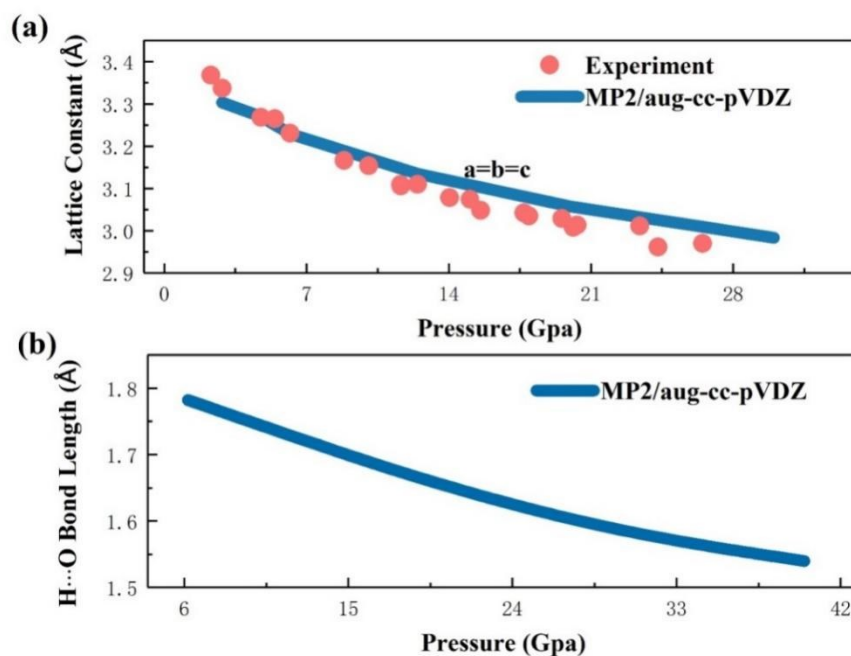
Figure S10 The pressure dependences of lattice constant (a) and H⋯O bond length (b) of ice VII. The blue curve is predicted by MP2/aug-cc-pVDZ, while the red dots are the experimental data from Walrafen *et al.* [17]
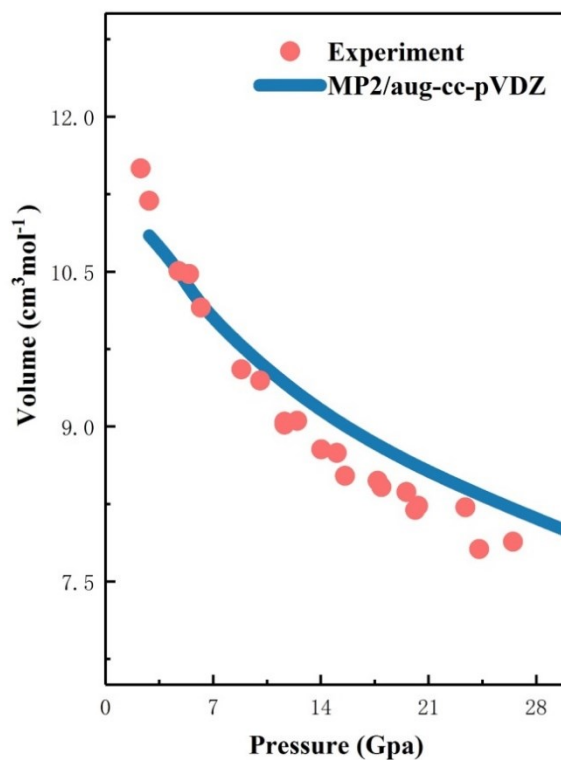
Figure S11 The pressure dependence of the unit cell volume of ice VII. The blue curve is predicted by MP2/aug-cc-pVDZ, while the red dots are the experimental data from Walrafen *et al.* [17].

Vibrational spectra

Ice VII is a proton-disordered structure, which results in the difficulty of vibrational spectral determination in the laboratory. In this case, the experimental data of Raman/IR spectra of ice VII is very scarce. Walrafen *et al.* [17] provided the Raman spectrum of ice VII at 3.2 GPa in the stretching frequency region, which is shown in the red curve of Figure S12, along with the MP2/aug-cc-pVDZ predicted result at the same pressure. The predicted two bands located between 3200 cm^{-1} and 3400 cm^{-1} agree well with the experiment, which demonstrates that the MP2 method is capable of providing accurate prediction of ice proton-disordered structures.
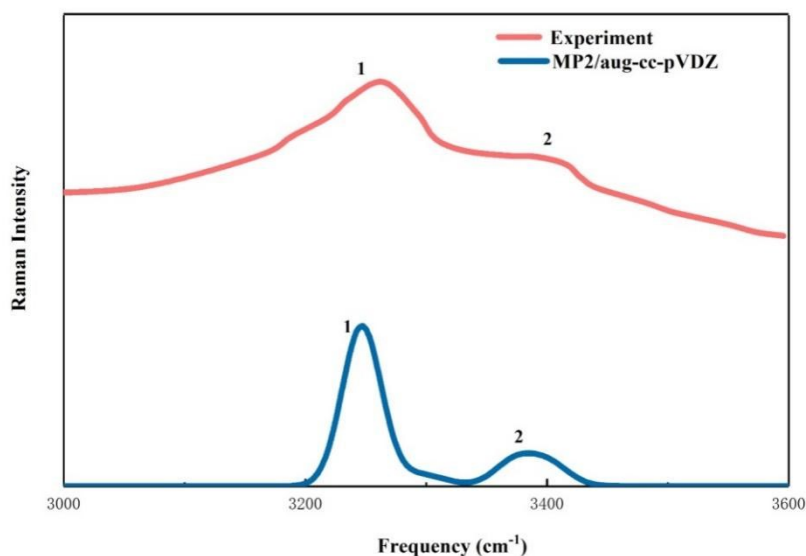
Figure S12 The predicted and observed Raman spectra of phase VII in stretching frequency region at 3.2 GPa. The observed spectrum is taken from Walrafen *et al.* [17].

4. Ice phase VIII

Crystal structure

Ice-VIII is known as a proton-ordered phase with a tetragonal unit cell. Ice VIII is formed from ice VII by lowering its temperature at about 5 °C (see the phase diagram of Figure 3). The proton ordering causes a slight distortion in the ice VII cubic lattice (*a,b* slightly shorter, *c* slightly longer) resulting in a tetragonal crystal structure of ice VIII (*I4$_1$/amd*). Figure S13 shows the unit cell of ice VIII. Similarly to ice VII, ice VIII consists of two interpenetrating cubic ice lattices. The molecular dipoles in these sub-lattices point to opposite directions along the *c* axis making the crystal antiferroelectric. The powder neutron diffraction measurement by Kuhs *et al.* [5] determined the structure of ice VIII at 2.4 GPa are: (*a,b,c,α,β,γ*)=(*4.449Å, 4.449Å, 6.413Å, 90°, 90°, 90°*) [5].
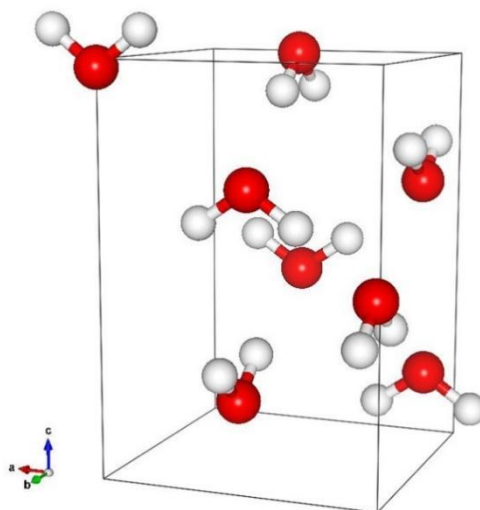
Figure S13 The unit cell (containing 8 water molecules) of Ice VIII, which is a proton-ordered, tetragonal structure with the space group of $I4_1/amd$. The lattice parameters are taken from Kuhs *et al.* [17].

Actually, it is possible that some different structures of ice VIII may exist, which possess variant proton directions. For example, Okada *et al.* [18] have introduced a new ferroelectric structure of ice VIII, where the molecular dipoles in the sub-lattices point in the same direction along the *c* axis making the crystal ferroelectric and thus the direction of protons has been changed. This structure is slightly less stable (~1 kJ/mol) than the antiferroelectric ice VIII, but is likely to exist during the proton ordered to disordered phase transitions, particularly in domains at high pressures. Furthermore, Klotz *et al.* [19] observed a low temperature metastable disordered ice form inside the stable region of proton-ordered ice VIII and suggested their thermal and pressure induced phase transition. Therefore, a metastable structure connecting ordered and disordered ice phases should exist to facilitate the ordered-disordered ice phase transition and support the great structural change. In the present study, the disordered ice structures (i.e., phase VI and VII) were selected based on their highest similarities of dipole moments to the corresponding ordered structures before phase transitions, rather than assuming that all configurations have the same statistical weight (as Pauling and many researchers did when estimating the free energies of ice) [20-22]. By doing this, we assume that in ice phase diagram before transforming into a completely different disordered phase, the ordered ice structure transits into an ensemble of disordered structures that have the close dipole moments with the neighboring ordered phase when the phase transition occurs.

Equations of state

Figure S14 plots the calculated and observed lattice constants and H···O bond length of ice VIII as a function of the pressure. The constants *a* and *b*, having the same length, undergo the same change with *c* as the pressure increases. The observed red dots, shown in Figure S14 (a), are taken from the work by Yoshimura *et al.* [23] and Besson *et al.* [24].The calculated pressure dependence of the ice VIII structural parameters (the blue curves in Figure S14) shows excellent agreement with the observed values.
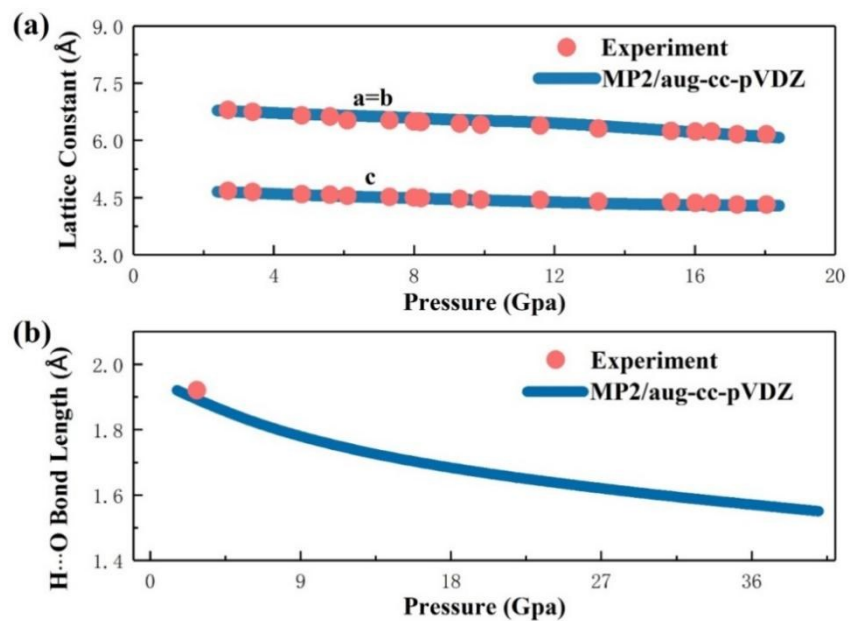
Figure S14 The pressure dependence of the lattice constant (a) and H···O bond length (b) of ice VIII. The calculation was performed at MP2/aug-cc-pVDZ level, while the observed lattice constants are adopted from the work by Yoshimura *et al.* [23] and Besson *et al.* [24]. The red dot in (b) denotes the observed H···O bond length of ice VIII at 2.8 GPa, which is taken from the work by Jorgensen *et al.* [25].
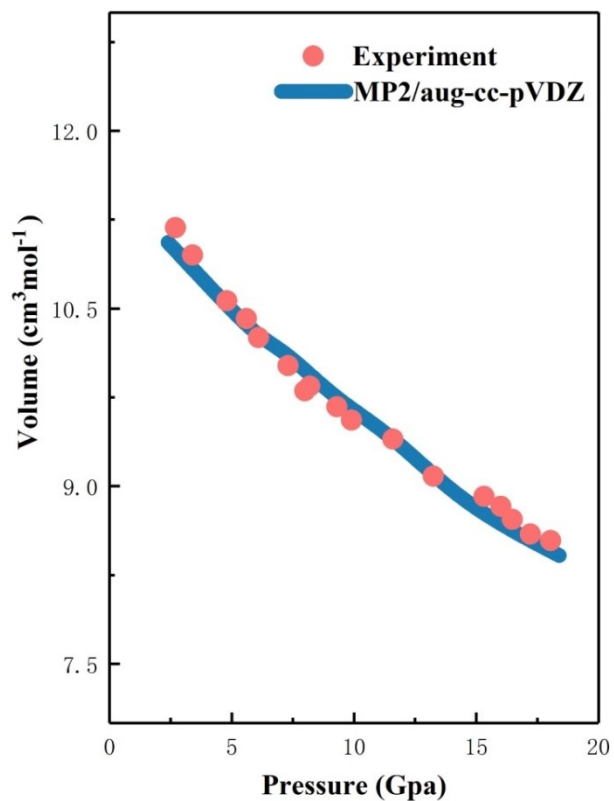
Figure S15 The pressure dependence of the unit cell volume of ice VIII. The predicted blue curve is calculated by MP2/aug-cc-pVDZ, and the red dots represent the experimental values adopted from the work by Yoshimura *et al.* [23] and Besson *et al.* [24].

Figure S15 compares the calculated unit cell volume of ice VIII with one set of observed data. The MP2/aug-cc-pVDZ result, gives accurate prediction of the volume of ice VIII, as compared to experimental data from 3 to 20 GPa. There is no discontinuity or any other anomaly in the calculated or observed volume.

Vibrational spectra

Vibrational spectrum is a distinct chemical fingerprint for a particular molecule or material, and can be used to rapidly identify the material, or distinguish them from others. The observed and calculated Raman and IR spectra are compared in the librational frequency region. Figure S16 shows the observed (red curve) and calculated (blue curve) Raman spectra of ice VIII at 2.8 GPa. In the librational region, ice VIII is predicted to display two Raman bands and one IR band at 2.8 and 2.25 GPa, respectively. The two predicted Raman bands are assigned to two observed bands in Figure S16, while the one IR band is assigned to one observed band in Figure S17. The good agreement of vibration spectra between MP2/aug-cc-pVDZ calculation and experiments renders the clear evidence that our MP2/aug-cc-pVDZ calculations are capable of reproducing the Raman and IR spectra of ice VIII with remarkable accuracy.
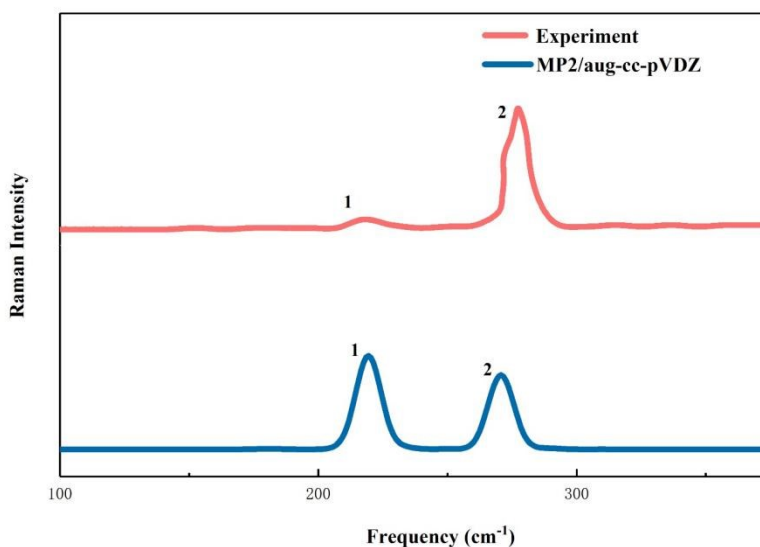
Figure S16 The observed (red curve) and calculated (blue curve) Raman spectra of ice VIII in the librational frequency region at 2.8 GPa. The observed spectrum is taken from Yoshimura *et al.* [23].
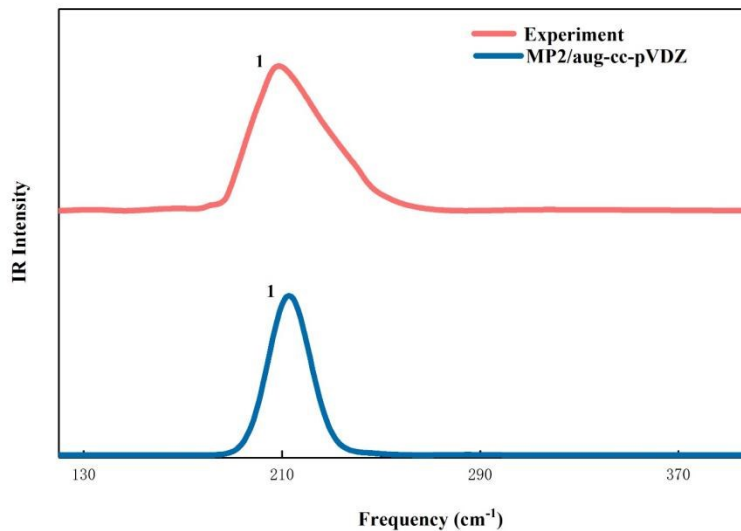
Figure S17 The observed (red curve) and calculated (blue curve) IR spectra of ice VIII at 2.25 GPa. The observed IR spectrum is taken from Klug *et al.* [26].

5. Ice phase IX

Crystal structure

Ice IX is low-temperature equilibrium, slightly denser structure with the space group of $P4_12_12$. It can be converted to ice II upon heating. Single crystal neutron diffraction experiment shows that ice IX has an almost completely proton-ordered structure, in which the ordered component contains two types of water molecules, type 1 in a site of no point symmetry, and type 2 on a twofold axis, each forming four hydrogen bonds in a three dimensional framework [24]. The crystal structure of ice IX was determined as: $(a,b,c,\alpha,\beta,\gamma)$=(*6.73Å, 6.73Å, 6.83Å, 90°, 90°, 90°*) [27].
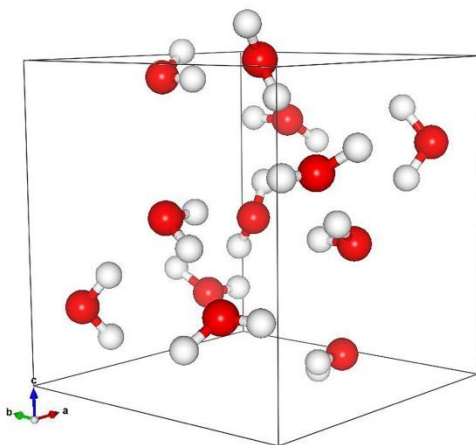
Figure S18 The unit cell (containing 12 water molecules) of ice IX, which is a proton-ordered, tetragonal structure with the space group of $P4_12_12$.

Equations of state
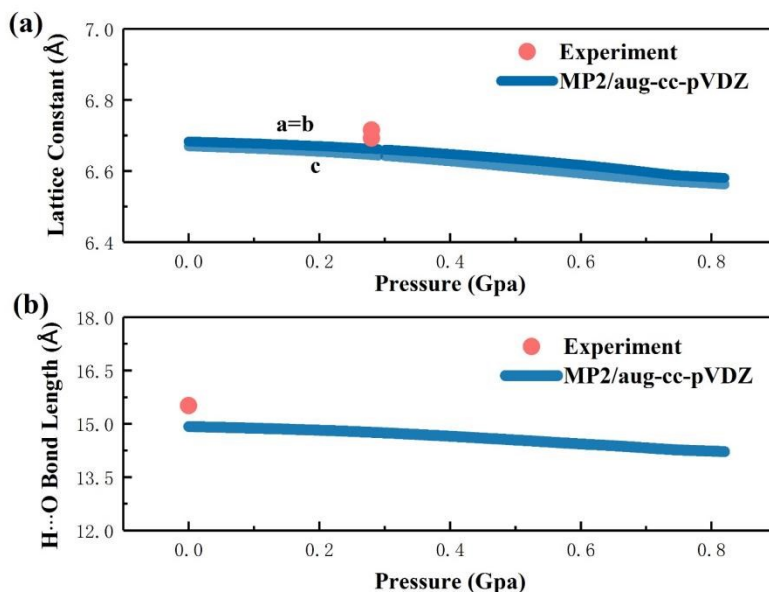
Figure S19 The calculated (blue curves) and observed (red dots) pressure dependence of the lattice constant (a) and the H···O bond length (b) of ice IX. The observed data are taken from Placa *et al.* [27] at 0.28 GPa.

The calculated pressure dependence of the ice IX's structural parameters also shows reasonable agreement with the observed results. The lattice constant and H···O bond length of ice IX as a function of the pressure are shown in Figure S19. The calculations were performed using MP2/aug-cc-pVDZ, while the observed data (red dots) are taken from the work by Placa *et al.* [27] Note that in addition to *a, b, c,* and *α, β, γ*, the H···O bond length in all ice phases have also been optimized at each pressure in our calculations, which, therefore, constitutes full optimization with only symmetry constraints imposed. Table S2 shows the comparison of calculated and observed lattice constants and volume of ice IX at atmospheric pressure. For ice IX, the MP2/aug-cc-pVDZ calculation predicts slightly more compact and stiffer solids at lower pressures than experiments.

Table S2 Comparison of calculated and observed lattice constants of ice IX at atmospheric pressure. The prediction was calculated by MP2/aug-cc-pVDZ, and the experimental data are taken from the work by Placa *et al* [27].

Ice IX	Experiment	MP2/aug-cc-pVDZ prediction
a (Å)	6.692	6.667
b (Å)	6.615	6.651
a/c	1.012	1.003

V (cm^{3}mol^{-1})	15.51	14.921

Vibrational spectra
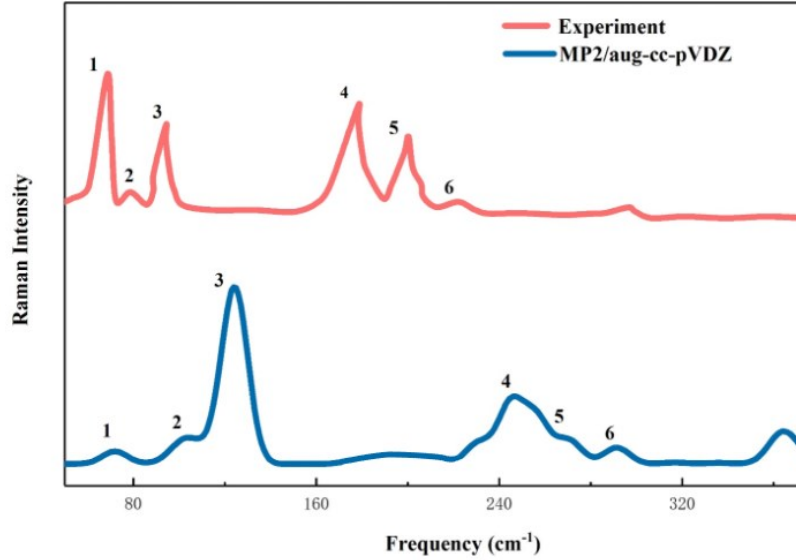
Figure S20 The observed [27] and calculated (using MP2/aug-cc-pVDZ) Raman spectra of ice IX in the librational frequency region at 0.28 GPa.

Figure S20 and Figure S21 compare the observed and calculated Raman and IR spectra of ice IX, respectively. Figure S20 gives the results at 0.28 GPa, while Figure S21 shows the spectra at atmospheric pressure. Ice IX at 0.28 GPa is predicted to display six Raman bands in the librational region, which are assigned to six observed bands labeled 1-6 in Figure S20. Ice IX also presents five IR bands, which are readily assignable to the bands labeled 1-5 in Figure S21. The experimental spectrum of the ice IX is obtained first [28], where only the oxygen atoms were verified to fit into space group, while hydrogen atoms did not. It was later proved that the hydrogen atoms also conform to the ordered structure of ice IX with the space group of P4$_1$2$_1$2$_1$ [27]. Therefore, the structure may be inconsistent, resulting in the spectra mismatch. In other words, there are obvious differences between the structure determined by the experimental spectra and the theoretical structure based on the experiment [27], leading to the inconsistency between the calculated peak density in observed and predicted (IR and Raman) spectra. Furthermore, when comparing with experimental spectra, due to the influence of experimental environment and theoretical factors, we care more about the number of peaks within a certain frequency range than the position of spectral peaks. As can be seen from Figures S20 and S21, the prediction and experiment matches well for the number of peaks, which provides a theoretical interpretation for the origin of the observed Raman and IR peaks of ice IX.
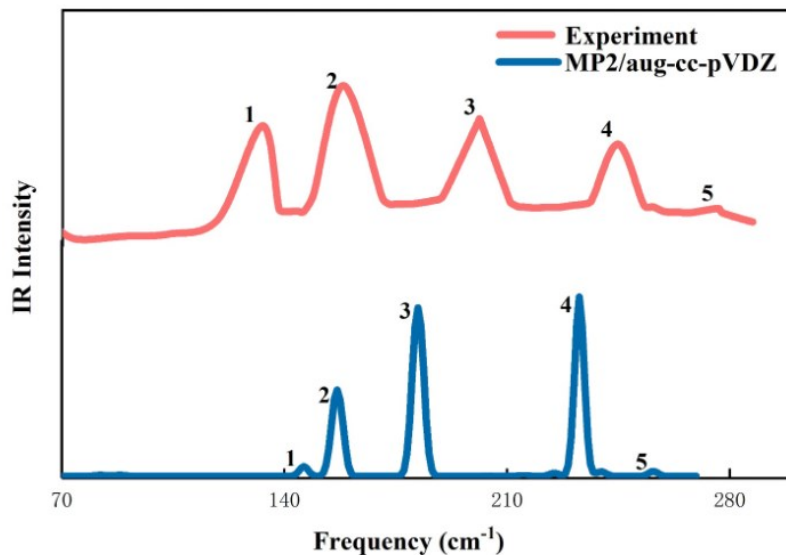
Figure S21 The observed [28] and calculated IR spectra of ice IX at atmospheric pressure.

6. Ice phase XV

Crystal structure

Ice XV is a slightly expanded proton-ordered form of the ice VI phase. Its existence was surmised based on the presence of the ordered forms of other ices at low temperatures. The structure and discovery of Ice XV are described by Salzmann *et al.* [29]. They observed neutron diffraction for ice XV prepared from ice VI by cooling slowly from 250 to 80 K at 0.2 K/min and ~0.9 GPa and found several additional peaks, which should have been absent owing to the symmetry of ice VI. The crystal structure of ice XV was determined as: ($a,b,c,\alpha,\beta,\gamma$)=(*6.2323 Å, 6.2438 Å, 5.7903 Å, 90.06°, 89.99°, 89.92°*), with the space group of $P\bar{1}$ [29].
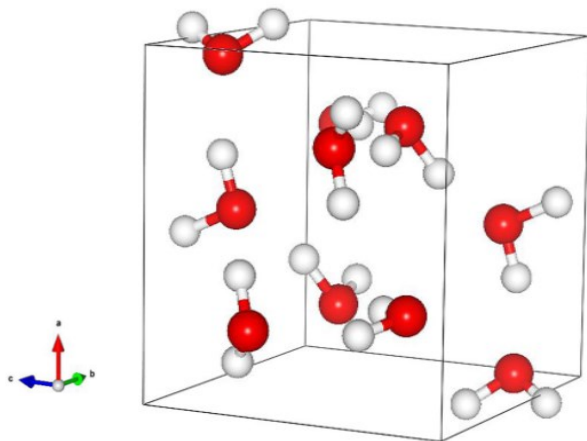
Figure S22 The unit cell of Ice XV, which contains 10 water molecules.

Equations of state
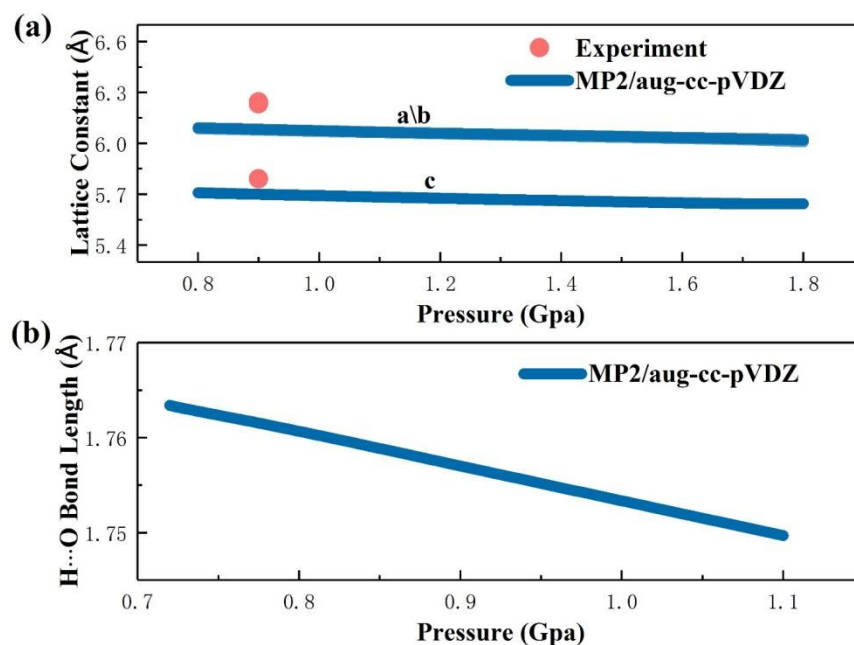
Figure S23 The pressure dependence of the lattice constants (a) and the H···O bond length (b) of ice XV. The prediction (blue curve) was calculated by MP2/aug-cc-pVDZ, while the observed lattice constants (red dots in (a)) are taken from the work by Salzmann *et al.* at 0.9 GPa [29].

Figure S23 plots the calculated lattice constants and H···O bond length of ice XV. The constant a, having the same length with b, undergoes the same amount of compression with c. As the pressure increases, the neighboring atoms experience sharp repulsive interactions of the nonbonded atom-atom potentials, which makes the structure stiffer and the potential energy curves of the crystal toward dissociation into separate individual hydrogen-bonded chains are anharmonic. At the low pressure, the solid is initially softer, shrinking easily under pressure. With increasing pressure, the solid becomes progressively stiffer, resisting compression. This is again explained by the fact that atoms enter the repulsive parts of the nonbonded potentials. The red dot shown in Figure S23 (a) is the observed data from Salzmann *et al.* at 0.9 GPa [29] Table S3 shows the comparison of calculated and observed lattice constants of ice XV at 0.9 GPa.

Table S3 Comparison of calculated and observed lattice constants of ice XV at 0.9 GPa. The prediction was calculated by MP2/aug-cc-pVDZ, and the experimental data are taken from the work by Salzmann et *al.* [29].

Ice XV	Experiment	MP2/aug-cc-pVDZ prediction
a (Å)	6.2323	6.0777
a (Å)	6.2438	6.0813
a/c	5.7903	5.6995

19

V (cm³mol⁻¹)	13.5533	12.7409

Vibrational spectra

In Figure S24, the observed and calculated Raman spectra of ice XV are compared in the range of 100-350 cm⁻¹. At 0.9 GPa, ice XV is predicted to display five Raman bands in the librational region, which are assigned to five observed bands labeled 1-5 in Figure S24.

But all positions of calculated spectral bands have an offset with the experiment and the density of calculated peak 3 differs obviously from the experiment. It could be inferred that the MP2 overestimated the frequency in the librational region and the weaker density of the calculated band 3 were associated with combinations of calculated band 2.
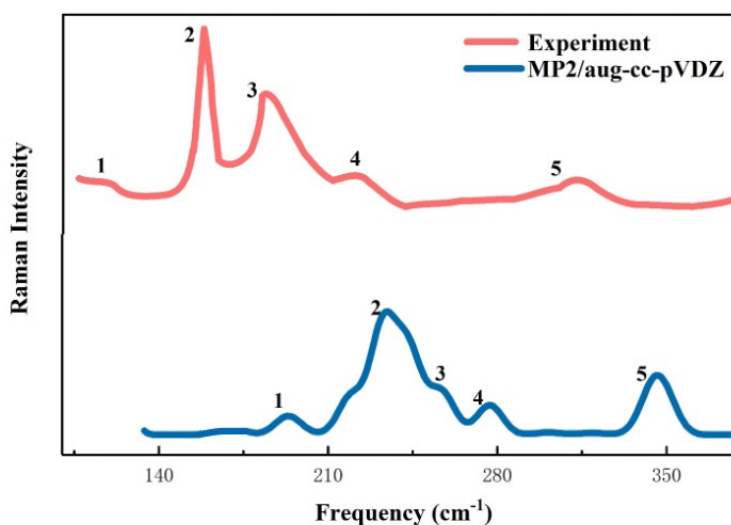
Figure S24 The observed [30] and calculated Raman spectra of ice XV in the librational frequency region at 0.9 GPa.

7. Vibrational frequency

Figure S25 and Figure S26 summarize the calculated and observed pressure-dependence of the frequencies of the Raman band positions. Since the phase diagram is dominated by ice VII and VIII when the pressure is above 3 GPa (shown in Figure 3), we separate the Raman band positions into two figures. Figure S25 shows the ice II, VI, IX and XV from 0 to 3 GPa, while Figure S26 depicts the Raman band positions of ice VII and VIII from 2 to 20 GPa. The majority of the modes of all ice phases experience increases in frequencies with the increasing pressure. MP2 calculation accurately reproduces the observed rates of frequency increasing with pressure.
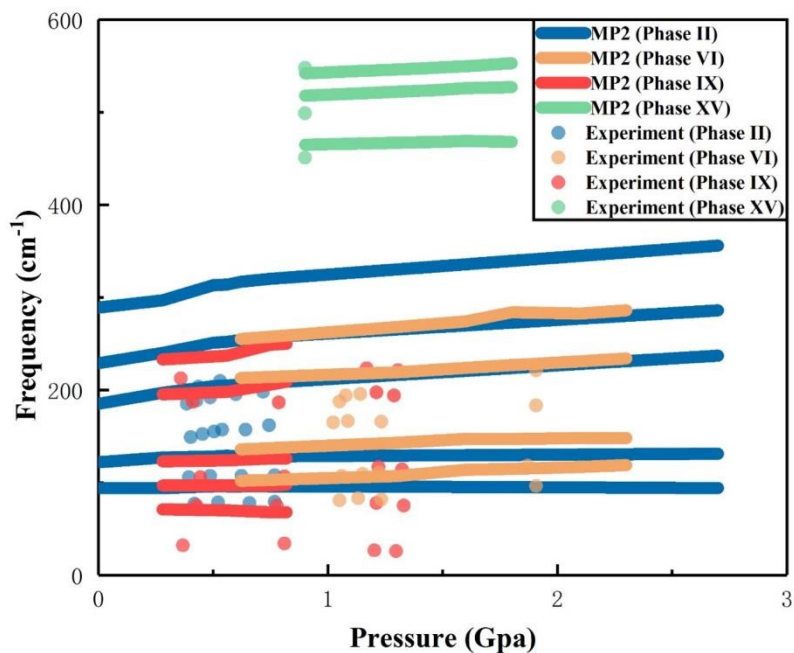
Figure S25 The pressure dependence of the Raman band position of ice II, VI, IX and XV within the observed range of 0-3 GPa. The observed data are taken from Wang *et al.* [30] and Whale *et al.* [31].
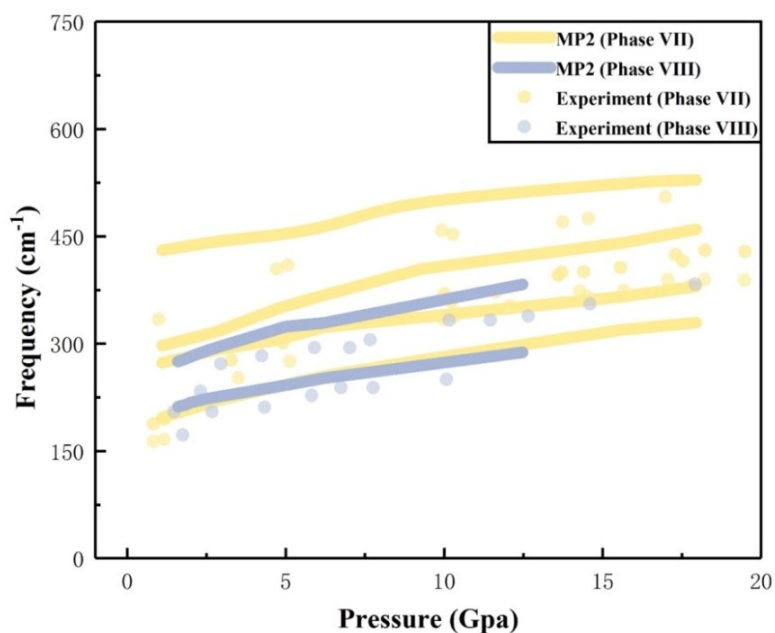
Figure S26 The pressure dependence of the band peak position of ice VII, VIII at high pressures. The observed peak positions are taken from Pruzan *et al.* [32] and Hirsch *et al.* [33].

8. Gibbs free energy differences

The calculated ice phase diagram (shown in Figure 3) is based on the Gibbs free energies, which tells us what the stable phases are at the given pressure and temperature. The major difficulty for theoretical prediction is the accuracy in calculation of the Gibbs free energy and entropy of all proton-disordered and ordered structures in phase diagram. None of the pioneering classical simulations and DFT predictions has shown the calculated results of Gibbs free energy differences of ice structures. Figure S27-Figure S35 show the Gibbs free energy differences of ices II-VI, VII-VIII, VI-XV, II-IX, VI-VIII, VI-VII, VI-IX, IX-XV, and VIII-XV as a function of temperature under difference pressures, calculated by MP2/aug-cc-pVDZ.
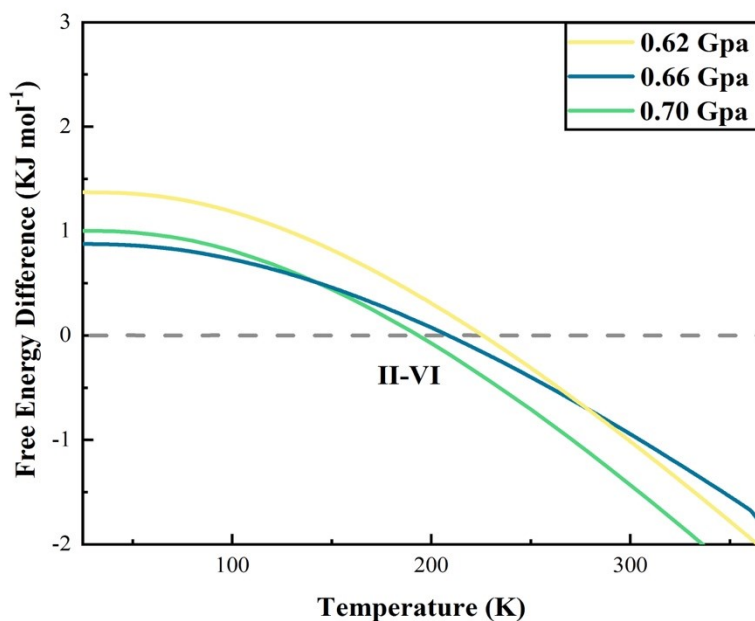
Figure S27 The calculated Gibbs free energy differences between ice II and VI as a function of temperature. The negative value means that ice II is more stable than ice VI.
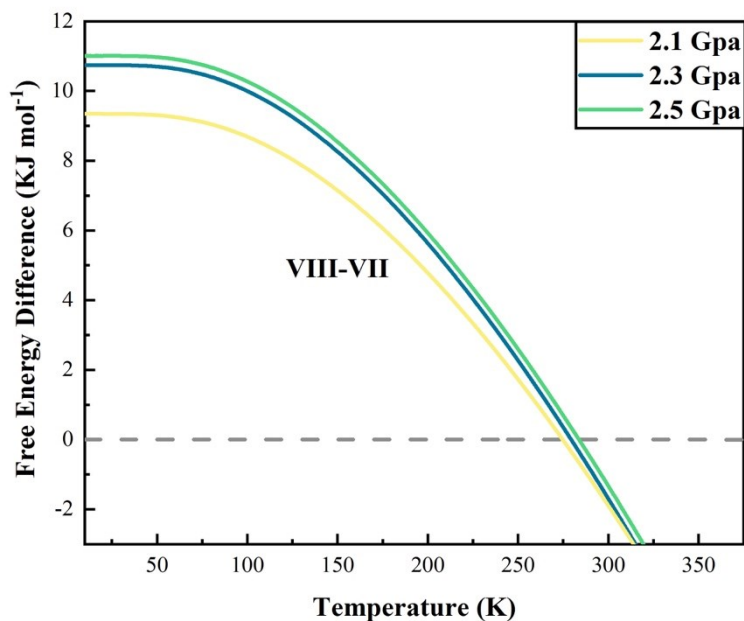
Figure S28 The calculated Gibbs free energy differences between ice VII and VIII as a function of temperature. The negative value means that ice VIII is more stable than ice VII.
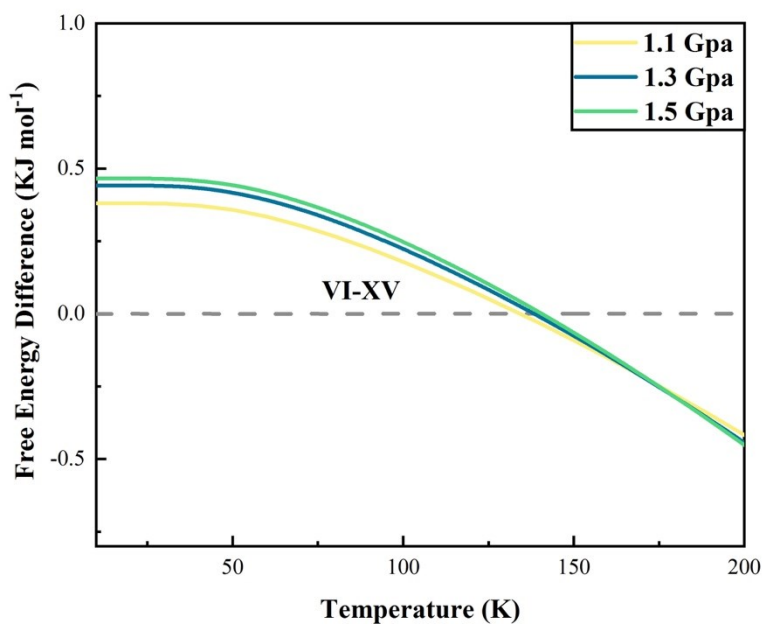
Figure S29 The calculated Gibbs free energy differences between ice VI and ice XV as a function of temperature. The negative value means that ice VI is more stable than ice XV.
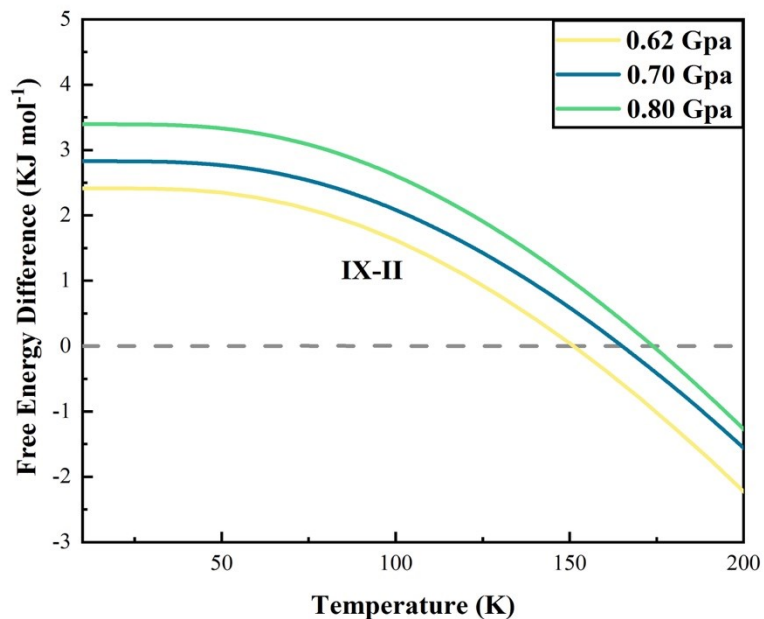
Figure S30 The calculated Gibbs free energy differences between ice II and ice IX as a function of temperature. The negative value means that ice IX is more stable than ice II.
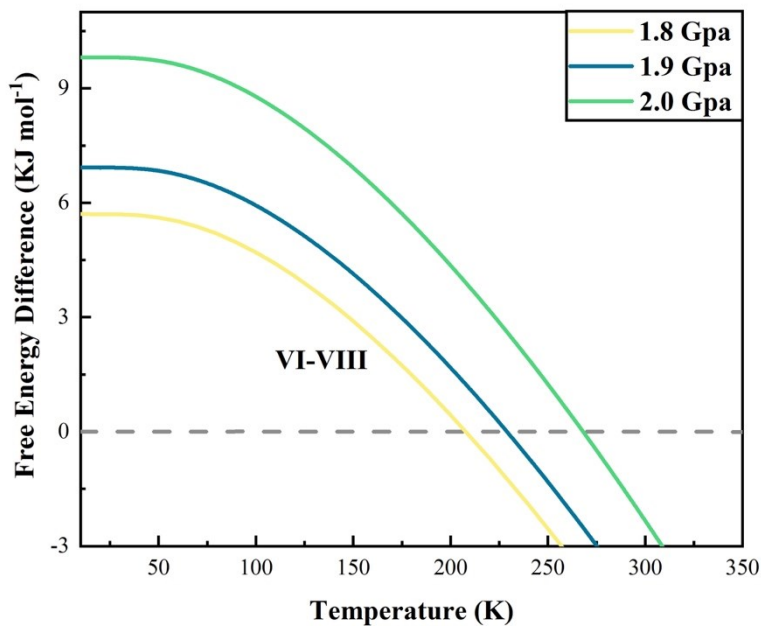
Figure S31 The calculated Gibbs free energy differences between ice VI and ice VIII as a function of temperature. The negative value means that ice VI is more stable than ice VIII.
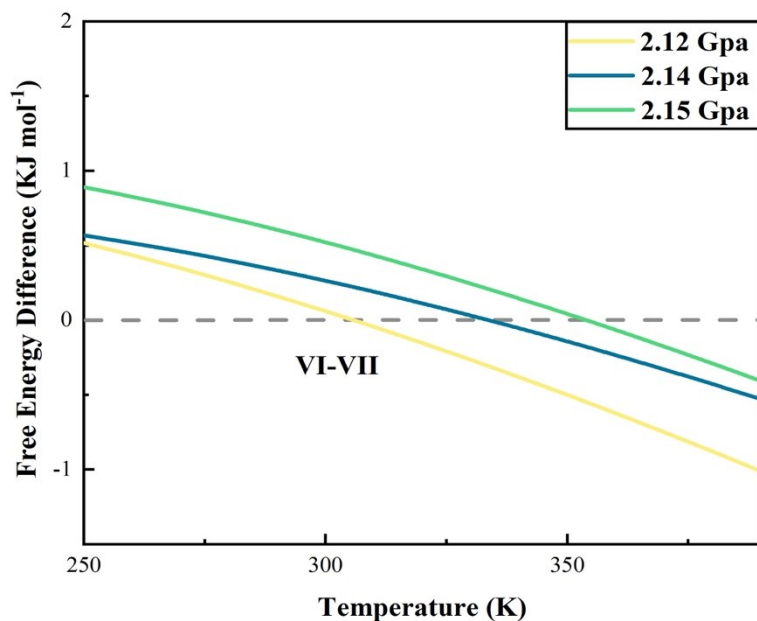
Figure S32 The calculated Gibbs free energy differences between ice VI and ice VII as a function of temperature. The negative value means that ice VI is more stable than ice VII.
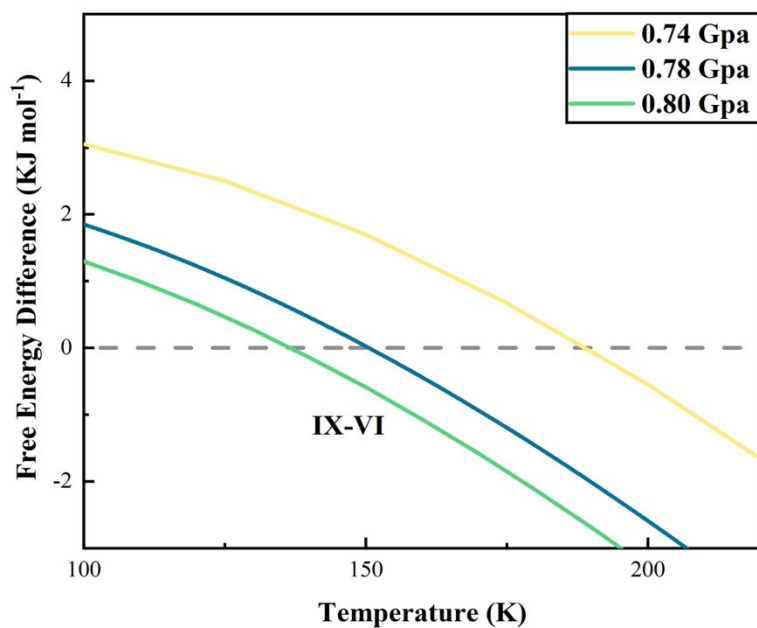
Figure S33 The calculated Gibbs free energy differences between ice VI and ice IX as a function of temperature. The negative value means that ice IX is more stable than ice VI.
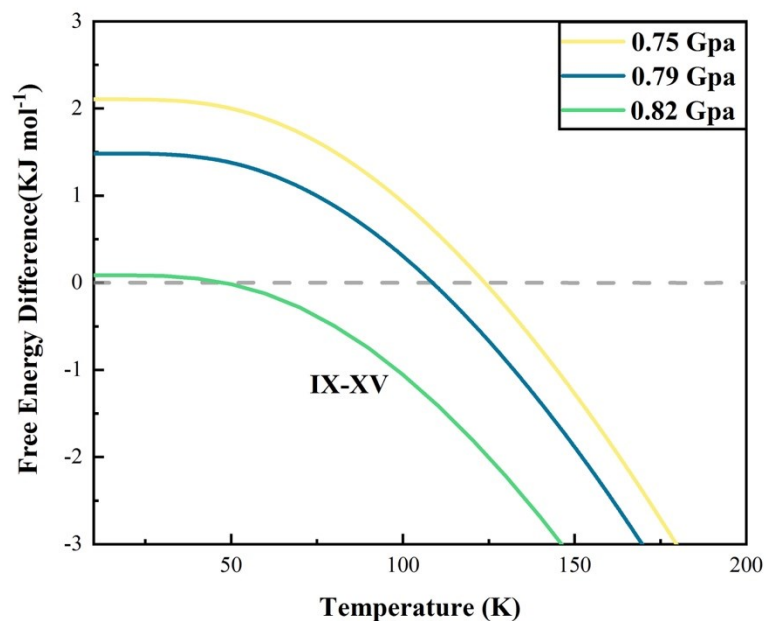
Figure S34 The calculated Gibbs free energy differences between ice IX and ice XV as a function of temperature. The negative value means that ice IX is more stable than ice XV.
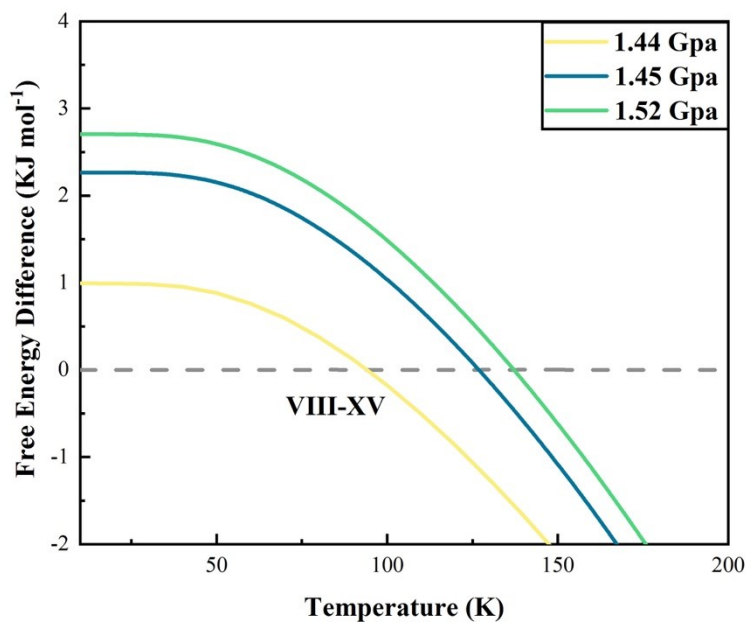
Figure S35 The calculated Gibbs free energy differences between ice VIII and ice XV as a function of temperature. The negative value means that ice VIII is more stable than ice XV.

9. Ice phase transitions
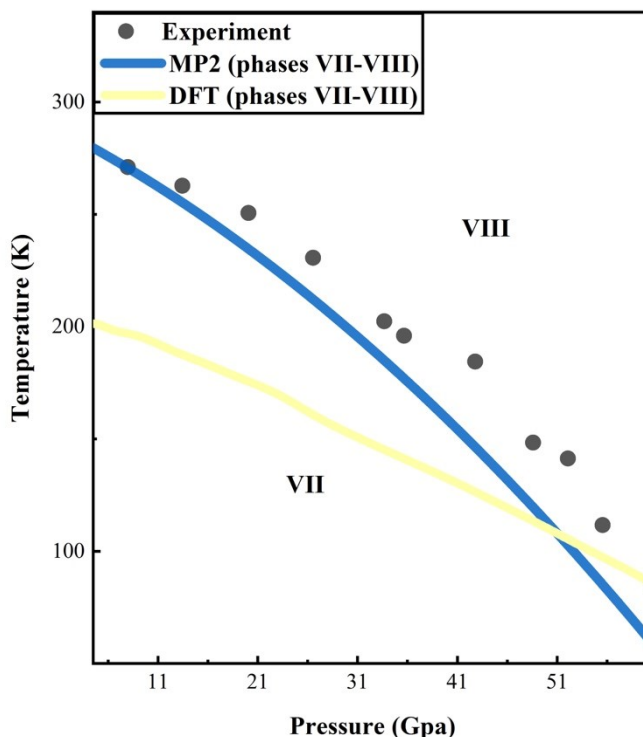
Figure S36 Comparisons of observed and calculated phase boundaries between ices VII and VIII. The black dots are experimental data taken from Pruzan *et al.* [34]. The yellow curve and blue curve are calculated results by DFT[35] and MP2/aug-cc-pVDZ, respectively. Our MP2 result is more in line with the observed phase boundaries.

We further plot the comparisons of observed and calculated phase boundaries of ice phases. Figure S36 shows the phase boundary between ice VII and ice VIII, where the black dots are experimental data taken from Pruzan *et al.* [34], the yellow curve is the predicted result by DFT calculation, and the blue curve is based on our MP2/aug-cc-pVDZ theory. Figure S36 shows that the phase boundary between ice VII and ice VIII predicted by MP2/aug-cc-pVDZ is in line with the experimental report, while exposing the limitation of the DFT calculation [35]*,* predicting a lower transition temperature and pressure. Figure S37 and Figure S38 are the comparisons of observed and calculated ice phase boundaries for phases II-VI and VI-VIII. The black curves are experimental data taken from Wang *et al.* [31]. The light blue and light pink curves are predicted results by SPC/E model (Figure S37) and T1P4P model (Figure S38), respectively, while the blue and pink curves are predicted by our MP2/aug-cc-pVDZ theory. The MP2 calculated phase boundaries of ice phases are uniformly in excellent agreement with experiments, surpassing the limitations of classical simulations and DFT calculations, which are still challenged by accurate descriptions of hydrogen bonding and van der Waals interactions and fail to reproduce the realistic ice phase diagram.
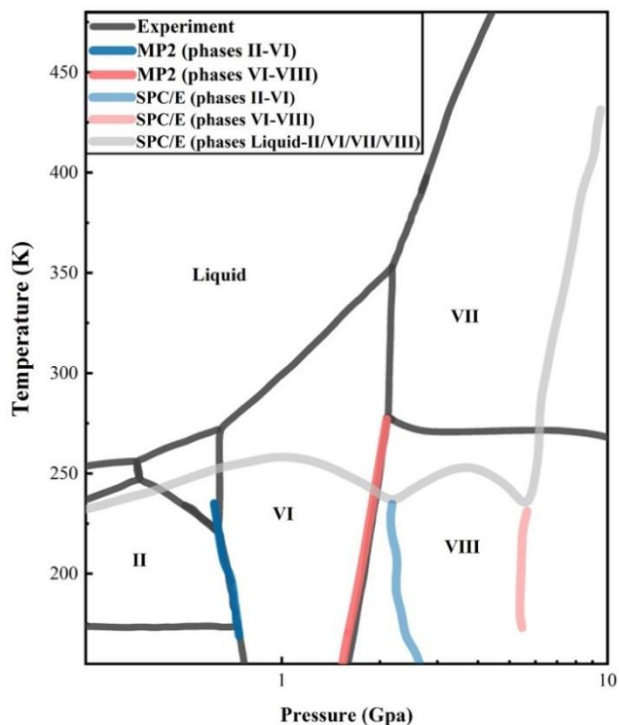
Figure S37 Comparisons of observed and calculated ice phase boundaries for phases II-VI and phases VI-VIII. The black curves are experimental data taken from Wang *et al.* [31]. The light blue and light pink curves are predicted by SPC/E model[62] and the blue and pink curves are predicted by MP2/aug-cc-pVDZ.

The MP2 predicted phase transition pressures and temperatures are shown in Table S4. With the increasing of pressure, the transition temperature exhibits several K more or less depending on Gibbs free energy differences.
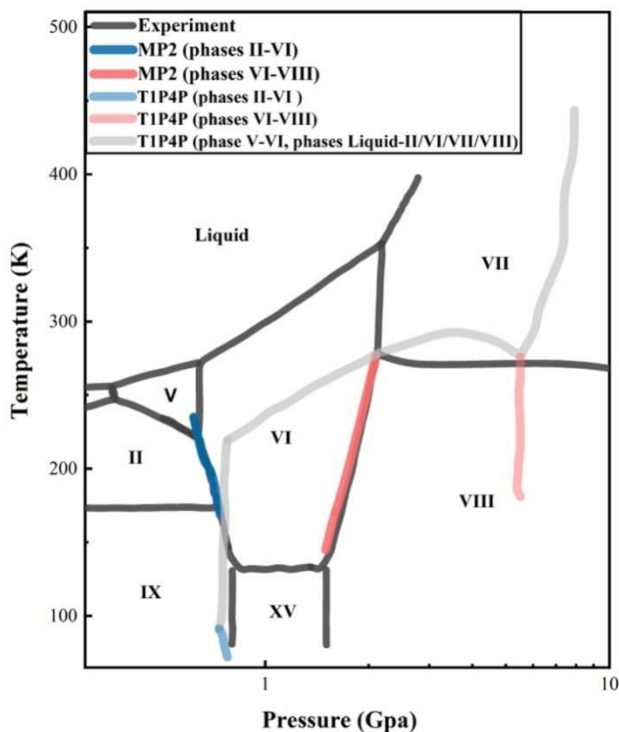
Figure S38 Comparisons of observed and calculated ice phase boundaries for phases II-VI and VI-VIII. The black curves are experimental data taken from Wang *et al.* [31]. The light blue and light pink curves are predicted by T1P4P model [36] and the blue and pink curves are predicted by MP2/aug-cc-pVDZ.

Table S4 The predicted phase transition pressures and temperatures for ices II, VI, VII, VIII, IX and XV, calculated by EE-GMF-MP2/aug-cc-pVDZ.

Transition phases		Transition pressure (GPa)	Transition temperature (K)
Phase VII	Phase VIII	2.3	278 ± 7
Phase VI	Phase VII	2.1	281 ± 8
Phase VI	Phase VIII	1.6	172 ± 7
Phase VI	Phase XV	1.15±0.35	136 ± 5
Phase XV	Phase VIII	1.46	79 ± 8
Phase IX	Phase XV	0.77	93 ± 6
Phase VI	Phase IX	0.78	155 ± 4
Phase II	Phase IX	0.62±0.12	165 ± 4
Phase II	Phase VI	0.66	208 ±7

References

[1] A.D. Fortes, I.G. Wood, J.P. Brodholt, and L. Vočadlo, *Ab initio* simulation of the ice II structure. *J. Chem. Phys.* **119**, 4567 (2003).

[2] B. Kamb, Ice. II. A proton-ordered form of ice. *Acta Cryst.* **17**, 1437(1964).

[3] B. Kamb, W.C. Hamilton, S.J. LaPlaca, A. Prakash, Ordered proton configuration in ice II from single-crystal neutron diffraction. *J. Chem. Phys.* **55**, 1934 (1971).

[4] J.E. Beritie, B.F. Francis, Raman spectra of ice II and IX above 35 K at atmospheric pressure: translational and rotational vibrations. *J. Chem. Phys.* **77**, 1(1982).

[5] W.F. Kuhs, J.L. Finney, C. Vettier, and D.V. Bliss, Structure and hydrogen ordering in ices VI, VII, VIII by neutron power diffraction. *J. Chem. Phys.* **81**, 361(1984).

[6] W.F. Kuhs, H. Ahsbahs, D. Londono, and J.L. Finney, In-situ crystal growth and neutron four-circle diffractometry under high pressure. *Physica B* **684,** 156 (1989).

[7] L. Pauling. The structure and entropy of ice and of other crystals with some randomness of atomic arrangement. *J. Am. Chem. Soc.* **57**, 2680 (1935).

[8] V. Buch, P. Sandler, J. Sadlej, Simulations of H_2O solid, liquid, and clusters, with an emphasis on ferroelectric ordering transition in hexagonal ice. *J. Phys. Chem. B* **102**, 8641 (1998).

[9] J.L. Aragones, L.G. MacDowell, and C. Vega, Dielectric constant of ices and water: a Lesson about water interactions. *J. Phys. Chem. A* **115**, 5745 (2011).

[10] L. Bezacier, B. Journaux, J.P. Perrillat, H. Cardon, M. Hanfland, I. Daniel, Equation of state of ice VI and ice VII at high pressure and high temperature. *J. Chem. Phys.* **141**, 104505(2014)

[11] B. Minceva-Sukarova, W.F. Sherman, G.R. Wilkinson, The Raman spectra of ice (Ih, II, III, VI and IX) as function of pressure and temperature. *J. Phys. C* **17**, 5833 (1984).

[12] J.E. Bertie, H.J. Labbé, E. Whalley, Infrared spectrum of ice VI in the range 4000-50 cm^{-1}. *J. Chem. Phys.* **49**, 2141-2144(1968).

[13] J.L. Kuo, M.L. Klein, Structure of ice-VII and ice-VIII: a quantum mechanical study. *J. Phys. Chem. B* **108**, 19634 (2004).

[14] P.V. Hobbs, Ice physics; Clarendon Press: Oxford (1974).

[15] V.F. Petrenko, R. W. Whitworth, Physics of ice; Oxford University Press: New York, (1999).

[16] O. Tschauner, S. Huang, E. Greenberg, V. B. Prakapenka, C. Ma, G.R. Rossman, A. H. Shen, D. Zhang, M. Newville, A. Lanzirotti, K. Tait. Ice-VII inclusions in diamonds: evidence for aqueous fluid in earth's deep mantle. *Science* **359**, 1136 (2018).

[17] G. E. Walrafen, Raman and x-ray investigations of ice VII to 36 GPa. *J. Chem. Phys.* **77**, 2166 (1982).

[18] F. Okada and K. Naya, Chapter 12: Electrolysis for ozone water production, in book of, Edited by J. Kleperis; *Publisher: IntechOpen* (2012).

[19] S. Klotz, J.M. Besson, G. Hamel, R.J. Nelmes, J.S. Loveday, W.G. Marshall, Metastable ice VII at low temperature and ambient pressure. *Nature* **398**, 681 (1999).

[20] L. Pauling, The structure and entropy of ice and of other crystals with some randomness of atomic arrangement. *J. Am. Chem. Soc.* **57**, 2680 (1935).

[21] V. Buch, P. Sandler, J. Sadlej, Simulations of H_2O solid, liquid, and clusters, with an emphasis on ferroelectric ordering transition in hexagonal ice. *J. Phys. Chem. B* **102**, 8641 (1998).

[22] J.L. Aragones, L.G. MacDowell, and C. Vega, Dielectric constant of ices and water: a lesson about water interactions. *J. Phys. Chem. A* **115**, 5745 (2011).

[23] Y. Yoshimura, S.T. Stewart, M. Somayazulu, H. Mao, R.J. Hemley, High-pressure x-ray diffraction and Raman spectroscopy of ice VIII. *J. Chem. Phys.* **58**, 567 (1973).

[24] J.M. Bession, Ph. Pruzan, S. Klotz, Variation of interatomic distance in ice VIII to 10 GPa. *Phys. Rev. B* **49**, 12540 (1994).

[25] J.D. Jorgensen, R.A. Beyerlein, N. Watanabe, T.G. Worlton, Structure of D_2O ice VIII from in situ power neutron diffraction. *J. Chem. Phys.* **81**, 3211 (1984)

[26] D. D. Klug, J. S. Tse, Z. Liu, X. Gonze, R. J. Hemley, Anomalous transformations in ice VIII. *Phys. Rev. B* **70**, 14413 (2004).

[27] S.J. La Placa, W.C. Hamilton, On a nearly proton-ordered structure for ice IX. *J. Chem. Phys.* **58**, 567 (1973).

[28] J.E. Bertie, H.J. Labbé, E. Whalley, Far-infrared Spectra of Ice II, V, IX. *J. Chem. Phys.* **49**, 775 (1968).

[29] C.G. Salzmann, P.G. Radaelli, E. Mayer, J. L. Finney, Ice XV: A new thermodynamically stable phase of ice. *Phys. Rev. Lett.* **103**, 105701 (2009).

[30] T. F. Whale, S.J. Clark, J.L. Finney, C.G. Salzmann, DFT-assisted interpretation of the Raman spectra of hydrogen-ordered ice XV. *J. Raman Spectrosc.* **44**, 290 (2013).

[31] Y. Wang, H. Zhang, X. Yang, S. Jiang, A. F. Goncharov, Kinetic boundaries and phase transformations of ice I at high pressure. *J. Chem. Phys.* **148**, 044508 (2018).

[32] P. Pruzan, J.C. Chervin, M. Gauthier, Raman spectroscopy investigation of ice VII and deuterated ice VII to 40 GPa, disorder in ice VII. *Europhys. Lett.* **13**, 81 (1990).

[33] K.R. Hirsch, W.B. Holzapfel, Effect of high pressure on the Raman spectra of ice VIII and evidence for ice X. *J. Chem. Phys.* **84**, 2771 (1986).

[34] P. Pruzan, J.C. Chervin, B. Canny, Determination of the D_2O ice VII-VIII transition line by Raman scattering up to 51 GPa. *J. Chem. Phys.* **97**, 718 (1992).

[35] K. Umemoto, R.M. Wentzcovitch, S.D. Gironcoli, S. Baroni. Order-disorder phase boundary between ice VII and VIII obtained by first principles. *Chem. Phys. Lett.* **499**, 236-240 (2010).

[36] E. Sanz, C. Vega, J. L. F. Abascal, L. G. MacDowell, Phase diagram of water from computer simulation. *Phys. Rev. Lett..* **92**, 4 (2004).